ISSN 1999-656X

Iraqi Journal of Applied Physics Letters

VOLUME (5) ISSUE (4) OCTOBER-DECEMBER 2022

Sponsored and Published by
Iraqi Society for Alternative and Renewable Energy Sources and Techniques

Co-published by
American Quality for Scientific Publishing

IRAQI JOURNAL OF APPLIED PHYSICS LETTERS

The *Iraqi Journal of Applied Physics Letters (IJAPLett)* is a peer reviewed journal of high quality devoted to the publication of original research papers from applied physics and their broad range of applications. IJAPLett publishes quality original research letters in physics and its applications in the broadest sense. It is intended that the journal may act as an interdisciplinary forum for physics and its applications. Innovative applications and material that brings together diverse areas of physics are particularly welcome. IJAPLett aims to disseminate knowledge; provide a learned reference in the field; and establish channels of communication between academic and research experts, policy makers and executives in industry, commerce and investment institutions. IJAPLett is a quarterly specialized periodical dedicated to publishing original letters in: Applied & Nonlinear Optics, Applied Mechanics & Thermodynamics, Digital & Optical Communications, Electronic Materials & Devices, Laser Physics & Applications, Plasma Physics & Applications, Quantum Physics & Spectroscopy, Semiconductors & Optoelectronics, Solid State Physics & Applications, Alternative & Renewable Energy, and Environmental Science & Technology.

ISSN (Print): 1999-656X, ISSN (Online): 2958-6488

EDITORIAL BOARD

Editorial Office:
P. O. Box 55259, Baghdad 12001, IRAQ
Website: www.iraqiphysicsjournal.com
Emails: editor@iraqiphysicsjournal.com, editor_ijap@yahoo.co.uk, ijap.editor@gmail.com,

ADVISORY BOARD

SPONSORED BY
IRAQI SOCIETY FOR ALTERNATIVE AND RENEWABLE ENERGY SOURCES AND TECHNIQUES (I.S.A.R.E.S.T.)
P. O. Box 55259, Baghdad 12001, IRAQ

PUBLISHED BY
AMERICAN QUALITY FOR SCIENTIFIC PUBLISHING INC.
1479 South De Gaulle Ct, Aurora,
CO 80018, United States

IRAQI JOURNAL OF APPLIED PHYSICS LETTERS

ISSN (Print): 1999-656x, ISSN (Online): 2309-1673

INSTRUCTIONS TO AUTHORS

CONTRIBUTIONS

Contributions to be published in this journal should be original research letters, i.e., those not already published or submitted for publication elsewhere, communications or letters to editor.
Manuscripts should be submitted to the editor at the mailing address:

Iraqi Journal of Applied Physics Letters, Editorial Board, P. O. Box 55259, Baghdad 12001, IRAQ
Website: www.iraqiphysicsjournal.com
Email: editor@iraqiphysicsjournal.com, editor_ijap@yahoo.co.uk, ijap.editor@gmail.com

MANUSCRIPTS

Two hard copies with soft Word copy on a CD or DVD should be submitted to Editor in the following configuration:

- **One-column** Double-spaced one-side A4 size with 2.5 cm margins of all sides
- Times New Roman font (16pt bold for title, 14pt bold for names, 12pt bold for headings, 12pt regular for text)
- Manuscripts presented in English only are accepted.
- Total number of words not exceed 2500 words and English abstract not exceed 100 words
- 4 keywords (at least) should be maintained on (PACS preferred)
- Author(s) should express all quantities in SI units
- Equations should be written in equation form (*italic* and symbolic) NOT in plain text
- Tables and Figures should be separated from text and placed in new pages after the references
- Charts should be indicated by the software used for generating them (e.g., Excel, MATLAB, Grapher, etc.)
- Figures and diagrams can be submitted in original colored forms for assessment and they will be returned to authors after provide printable copies
- Only original or high-resolution scanner photos are accepted
- For electronic submission, articles should be formatted with MS-Word software.

AUTHOR NAMES AND AFFILIATIONS

It is IJAPLett policy that all those who have participated significantly in the technical aspects of a paper be recognized as co-authors or cited in the acknowledgments. In the case of a paper with more than one author, correspondence concerning the paper will be sent to the first author unless staff is advised otherwise.
Author name should consist of first name, middle initial, last name. The author affiliation should consist of the following, as applicable, in the order noted:
- Company or college (with department name or company division), Postal address, City, Governorate or State, zip code, Country name, contacting telephone number, and e-mail

REFERENCES

The references should be brought at the end of the article, and numbered in the order of their appearance in the paper. The reference list should be cited in accordance with the following examples:
[1] X. Ning, R. Benford and M.R. Lovell, "On the Sliding Friction Characteristics of Unidirectional Continuous FRP Composites", *J. Tribol. Func. Mater.*, 124(1) (2002) 5-13.
[2] M. Barnes, "Stresses in Solenoids", *J. Appl. Phys.*, 48(5) (2001) 2000–2008.
[3] J. Jones, **"Contact Mechanics"**, Cambridge University Press (Cambridge, UK) (2000), Ch.6, p.56.
[4] Y. Lee, S.A. Korpela and R. Horne, "Structure of Multi-Cellular Natural Convection in a Tall Vertical Annulus", Proceedings of 7th International Heat Transfer Conference, U. Grigul et al., eds., Hemisphere (Washington DC), 2 (1982) 221–226.
[5] M. Hashish, "Waterjet Technology Development", High Pressure Technology, PVP-Vol. 406 (2000) 135-140.
[6] D.W. Watson, "Thermodynamic Analysis", ASME Paper No. 97-GT-288 (1997).
[7] C.Y. Tung, "Evaporative Heat Transfer in the Contact Line of a Mixture", Ph.D. thesis, Rensselaer Polytechnic Institute, Troy, NY (1982).

PROOFS

Authors will receive proofs of papers and are requested to return one corrected copy as a WORD file on a compact disc (CD) or by email. New materials inserted in the original text without Editor's permission may cause rejection of paper unless the handling editor is informed.

COPYRIGHT FORM

Author(s) will be asked to sign the IJAPLett Copyright Form and hence transfer copyrights of the article to the Journal soon after acceptance of it. This will ensure the widest possible dissemination of information.

OFFPRINTS

Authors will receive electronic offprint free of charge and any additional reprints can be ordered.

SUBSCRIPTION AND ORDERS

Annual fees (4 issues per year) of subscription are:
50 US$ for individuals inside Iraq; **200** US$ for institutions inside Iraq;
100 US$ for individuals abroad; **300** US$ for institutions abroad.

Enhanced Corrosion Resistance of Titanium-Cobalt Alloys Coated by Alumina Using Plasma Sputtering

Zainab T. Abdulhamied, Shahlaa Jomaa, Aqeel F. Hassan

Ministry of Science and Technology, Baghdad, IRAQ

Abstract

In this study, plasma sputtering technique was used to enhance the yearly corrosion average of alumina to be about $2.21x10^{-4}$ mpy on Ti-20%Co alloy. The Ti-Co alloy is popularly used for surgical implant because it has good mechanical properties, high degree of biocompatibility, bioinert and osseo-integrations with bones. This research is focusing on different sputtering parameters such as the discharge voltage, sputtering time and gas pressure. A good result was found when a 1200 V is applied on the electrodes for 4 hours under $4x10^{-3}$ mbar argon gas pressure. The electrochemical tests of the Ti-20%Co alloy were also performed before and after coating in simulated body fluids. The average corrosion rate of alloy before coated was $1.98x10^{-2}$ mpy, while the average corrosion rate after coted Al_2O_3 was about $2.21x10^{-4}$ mpy at 1200 V.

Keywords: Plasma sputtering; Ti-Co alloys; Corrosion; Ceramics; Biomaterials; Biomedical applications
Received: 2 May 2022; **Revised:** 4 July 2022; **Accepted:** 11 July 2022; **Published:** 1 October 2022

1. Introduction

Sputtering comes from the operation of the collision between accelerating particles towards the target. The exchange operating between particles and target atoms of the upper layer in specimens. The number of sputtering atoms depends on the angle fall of the bombing particle.it is increasing with many factors started with the cosine fall angle, mass bombing particle, speed. when particle falls and colliding vertically with the target atom, so the atom diffusion inside the target away from the surface, yet there will be no sputtering these collisions accrue a different atomic levels inside the crystalline material that causes a loss in the ionic energy some atoms obtain energy through inflexible collisions because of many atomic levels deep in the material the atoms acquire different energies, the atoms can escape from upper level when they have a larger energy. The dropping iconic energy, but the atom exists on the far levels suffers from many collisions neighboring atoms then loss many energies and escape the surface target. This energy sputtering will be fewer than the sputtering atom energy on the target surface [5-7].

The characteristics of alumina is a strong ionic bonds, density about 3.95 g/cm^3,the hexagonal phase α-Al_2O_3 is considered more stable from other phases is called Corundum which is widely using in applications because of its high hardness, good thermal and high electrical insulation. Alumina (Al_2O_3) has two phases white crystalline structure (physical and chemical) properties are called phase α and phase y [10]. It has been noticed that α-Al_2O_3 is looked like white crystals not inclined humidity it exists naturally in the Corundum metal. Table (1) shows the most common properties of aluminum oxide.

Table (1) properties of aluminum oxide [11]

Aluminum Oxide (Alumina)	
Chemical formula	Al_2O_3
Molar Mass	101.96 g/mol
Density	4.05 g/cm^3
Melting point	2054 ºC
Solubility in water	Negligible

When the aluminum hydroxide is heated under 400°C γ-aluminum oxide, it seems white smooth powder and disintegrates in acids and moves to phase α-aluminum when heating to it under 950°C. Also, that γ-aluminum characterize of its good portability of absorption so this is why it is used during operations and removal colors of solutions [8,9]. Surface modifications of materials provide the base for achieving specific

material properties for specific applications. The main advantage of laser surface modification is the ability to improve the properties of different materials [12]. The performance and applications of biomaterials in biological systems are of critical importance for the development of biomedical implants and tissue engineering. There are numerous biomaterials that can be used in the human body, such as metals e.g. stainless steel, cobalt alloys, titanium alloys), ceramics (aluminum oxide, zirconia, calcium phosphates), and synthetic and natural polymers [13]. Table (2) summarizes the medical and biomedical applications of some ceramic materials.

Titanium is a reactive material and has an very high affinity for oxygen, which means that the protective oxide film forms spontaneously and instantly and its disruption or damage is repaired immediately [9], if the metal is in the presence of air or oxidizing media, as is the case in a biological system when a bio-liquid surrounds the metal [17].

Table (2) Medical and biomedical applications of some ceramic materials [3]

Ceramic		Applications
Alumina	Al_2O_3	Cutting tools, dies, wear, resistant parts and coating, oxidation barriers, bearing surfaces, high temperature components, turbine parts, hip implants, body armor, radiation shielding.
Silicon Carbide	SiC	
Silicon Nitride	Si_3N_4	
Zirconium	ZrO_2	
Boron Nitride	BN	

2. Materials and methods

For the purpose of studying the exact structure of the alloy use an etching solution is made from (H_2O10ml.HCl:5ml HNO_3:15ml) specimen immerses for 5 second with the etching material that is followed by washing the specimens with the dropping water then the operation drying specimens, the microscopic examination shows two phase in all main shapes in the alloy, moreover the base structure which formers from (β-Ti) with cubic body center bcc. The result of the exact examination for the untreated alloy on the Alfa grains in the Beta flooring. And found structure (α and ß) is distinguished the best properties and it is used in the application of the surgical implants [14].

It was depended on the electrochemical method for measuring the corrosion rate of the base alloy, the specimens are coating with alumina. The tests were done by using potential which was made laboratory by water bath method with fixed temperature of liquid about 37±1°C to simulate the temperature of the human body [12].

The way of drawing the polarization curve potential stress, at first it depends on the determination of potential value between the work pole and comparative pole when there is no current in the outer circuit, whenever the value of current equal zero, the circuit will be open and this is called corrosion potential or open circuit potential [10]. Also that determinate the open circuit potential for the coated and uncoated specimens of the alloy. We need to immersion these specimens in SBF solution which was laboratory prepared for finding the equilibrium between the specimens and the electrolytic solution. The value of the changes in potential with time was read for half-an hour for each specimen. Figure (1) illustrates (OCP) for the specimens before and after coating with different times. The result shows a passive thin layer which covers the alloy through immersion it in SBF solution which was stable after a very short time and it is found to move and getting closer towards the behavior of the noble element.

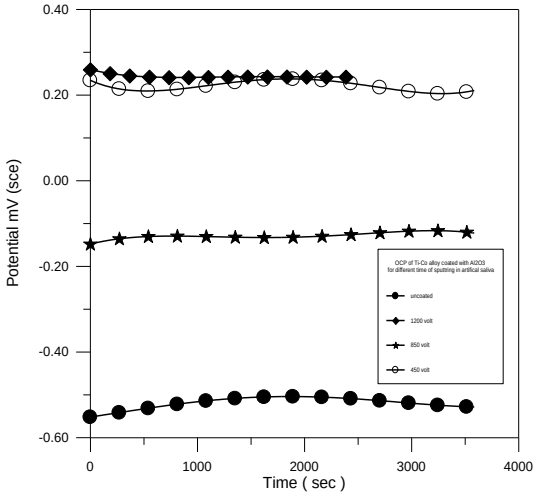

Fig. (1) Open-circuit potential (OCP) for Ti-20%Co alloy coated and uncoated by sputtering with Al_2O_3 and argon gas pressure $4x10^{-2}$ mbar

Figure (2) shows polarization curve for base alloy before coating in SBF solution which is prepared laboratory. It has been determined the influencing parameters in the behavior corrosion, which are value of corrosion current and corrosion potential, by using Tafel extrapolation and through the fixed program in the Potential Stress device.

The Tafel curve in Fig. (2) showed that the base alloy (TiCo) has a corrosion current density I_{corr} ($1.37x10^{-6}A/cm^2$) which is coincided with the value of current density for the most of Titanium alloys in the same corrosion middle (SBF) [15,16],yet the value of corrosion potential E_{corr} was (-905mv) while the average corrosion of alloy was $1.98x10^{-2}$ mpy.

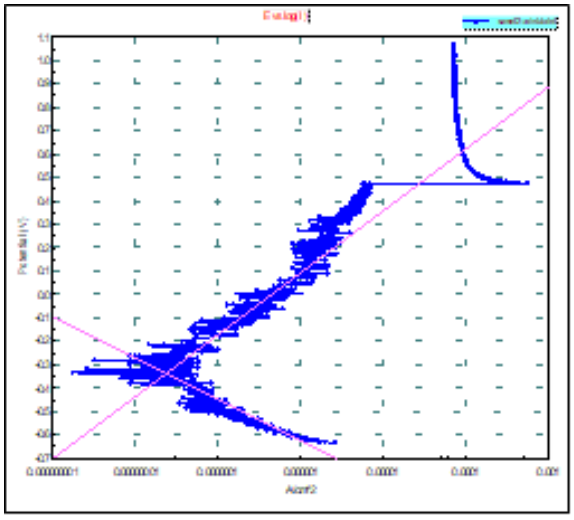

Fig. (2) The polarization curve of uncoated base alloy in SBF

The specimens are coated with alumina seen in figures (3-5) by polarization curves for Ti-20%Co alloy are coated with Alumina and with different sputtering volts (450, 850 and 1200 V). The coated alloy under 1200 V and (the thickness of the layer is 0.41mm) showed less resistant for the corrosion in a comparison with the base alloy and it is obvious from the high corrosion current value from corrosion value of base alloy equals I_{corr} ($2.35x10^{-2}$ $\mu A/cm^2$), E_{corr} (-337.2mV) and the yearly corrosion average is about ($2.21x10^{-4}$ mpy).

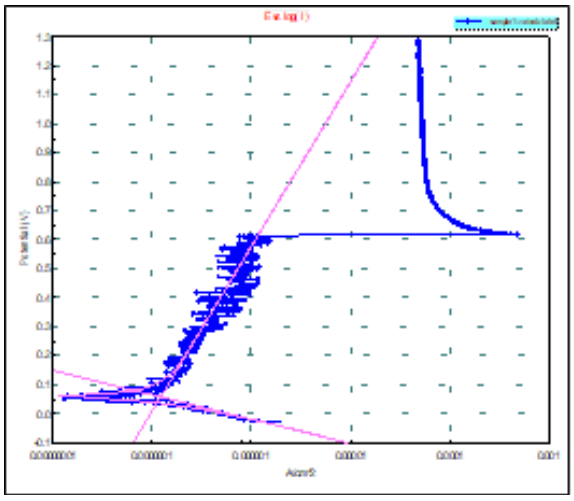

Fig. (3) The polarization curve of coated base alloy with Al_2O_3 at 450 volt in SBF

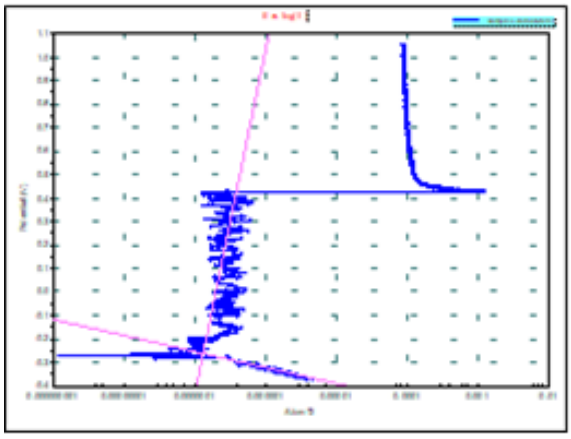

Fig. (4) The polarization curve of coated base alloy with Al_2O_3 with 850 volt in the SBF

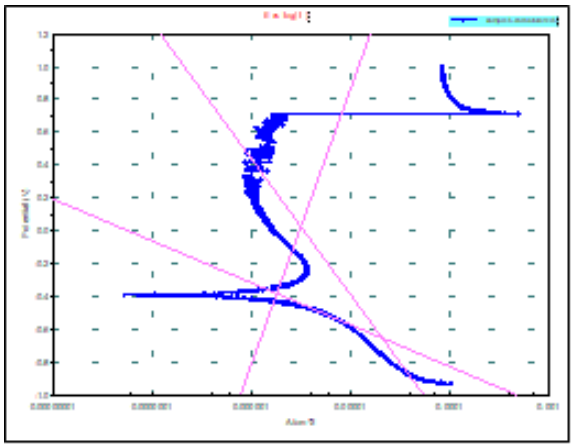

Fig. (5) The polarization curve of coated with Al_2O_3 at 1200V in SBF

It is obvious that all the figures shows corrosion resistance for coated specimen with sputtering volts 850 volt and coated layer thickness about 0.3 mm was recorded for $1.321x10^{-1}$ $\mu A/cm^2$, Whereas the average

corrosion yearly is $1.242x10^{-3}$ mpy. We notice that for the specimen coated at volts 450 volt, coated layer thickness 0.25 mm. The corrosion current equal to 1.086 μA/cm^2 and the average corrosion yearly ($1.698x10^{-2}$ mpy), while the corrosion potential of the coated specimens range E_{corr} (-363.7,-262.6 mV), respectively.

4. Conclusions

The results indicated that Ti-Co developed a more stable passive layer than the other alloys. This is due to thick Al_2O_3 layers that help create a passive layer that is more resistant to corrosion. The results show the clearly increasing in the sputtering voltage leads to increasing the layer thicknesses at the same time, all optical microscopic pictures shows homogenous Al_2O_3 thick films on Ti-Co alloy surface, also we found the base structure which formers from β-Ti with cubic body center in white color with deep color for α-Ti phases. In corrosion test we fixed temperature at 37°C for SBF, in OCP test we show passive thin layer covers the alloys after immersion in SBF which was stable after a very short time and its behavior of the noble element.

References

[1] D. Bochenek, "Advanced Ceramic Materials with Functional Properties", *Materials*, 15 (2022) 6439.

[2] J.R. Kelly and P. Benetti, "Ceramic materials in dentistry: historical evolution and current practice", *Australian Dent. J.*, 56(1) (2011) 84-96.

[3] P.K. Davies and R.S. Roth, "Chemistry of Electronic Ceramic Materials", NIST Special Publication, 804 (1990).

[4] R. Elo, S. Jacobson and T. Kubart, "Tailoring residual stresses in CrN_x films on alumina and silicon deposited by high-power impulse magnetron sputtering", *Surf. Coat. Technol.*, 397 (2020) 1259.

[5] B. Kohlhauser et al., "How microalloying of the Al target can improve process and film characteristics of sputtered alumina", *Surf. Coat. Technol.*, 393 (2020) 125762.

[6] A.M. Titu, B. Miao and A.B. Pop, "Special Issue: Surface Modification of Magnesium, Aluminum Alloys, and Steel", *Coatings*, 12 (2022) 1349.

[7] D.R. Unune, G.R. Brown and G.C. Reilly, "Thermal based surface modification techniques for enhancing the corrosion and wear resistance of metallic implants: A review", *Vacuum*, 203 (2022) 111298.

[8] N. Llorca-Isern and O. Rius-Ayra, "Specia Issue: Surface Modification of Metals and Alloys" *Coatings*, 11(2) (2021) 260.

[9] N. Cui, S. Chen and T. Xu, "The Microstructure, Mechanical Properties, and Corrosion Resistance of a Novel Extruded Titanium Alloy", *Metals*, 12 (2022) 1564.

[10] X. Geng, J. Jiang and X. Zhang, "Corrosion Behavior of $Mg_{-x}Gd_{-1}Zn_{-0.4}Zr$ Alloys with Different Gd Additions for Biomedical Application", *Metals*, 12(10) (2022) 1763.

[11] H.N. Åhman and F. D'Elia, "Microstructural Origins of the Corrosion Resistance of a Mg-Y-Nd-Zr Alloy Processed by Powder Bed Fusion–Laser Beam", *Front. Bioeng. Biotechnol.*, 01 July 2022, doi: 10.3389/fbioe.2022.917812.

[12] J. Sypniewska, "Influence of Laser Modification on the Surface Character of Biomaterials: Titanium and Its Alloys - A Review", *Coatings*, 12 (2022) 1371.

[13] B.T. Lee, A.K. Gain and H.Y. Song, "Fabrication of Porous Al_2O_3 and ZrO_2 Ceramics and Evaluate their Biocompatibility", *Euro. Cells Mater.*, 11(Suppl. 1) (2006) (page 47).

[14] S. Chitra et al., "Strategies of Bioceramics, Bioactive Glasses in Endodontics: Future Perspectives of Restorative Dentistry", *BioMed Res. Int.*, Volume 2022, Article ID 2530156.

[15] K.D. Weltmann, "Biomedical applications of atmospheric pressure plasma", *Chem. listy*, 102 (2008) 1450-1451.

[16] X. Liu, P. Chu and C. Ding, "Surface modification of titanium, titanium alloys, and related materials for biomedical applications", *Mater. Sci. Eng. R*, 47 (2004) 49-121.

[17] F. Almeraya-Calderón and J.M. Jáquez-Muñoz, "Corrosion Behavior of Titanium and Titanium Alloys in Ringer´s Solution", *Int. J. Electrochem. Sci.*, 17 (2022).

Optical Properties of Nanostructured MgO:TiO_2 Thin Films Prepared by Sol-Gel Technique

Amel S. Suber, Hanaa K. Khalaf, Seham Z. Abbas, Mohammed E. Ismael

Directorate of Materials Research, Ministry of Science and Technology, Baghdad, IRAQ

Abstract

In this paper, the optical properties of MgO and MgO:TiO_2 nanostructured thin films grown on quartz substrates by sol-gel (dip-coating) are studied. It should be noted that the thickness of the deposited film was about 250nm. The films were heated in air at 550°C for 3 hours. The results showed that the impurities cause a decrease in the transmittance and energy band gap of (from 4 to 3.68eV). The films were examined for their ability to detect NH_3 gas at 6 ppm at room temperature by measuring their sensitivity to this gas at various times.

Keywords: Thin films; Sol-gel; magnesium oxide; Titanium dioxide; Gas sensors
Received: 3 May 2022; **Revised:** 5 July 2022; **Accepted:** 12 July 2022; **Published:** 1 October 2022

1. Introduction

Due to its wide energy band gap, good chemical properties, thermal stability, and optical properties, magnesium oxide (MgO) is a particularly promising candidate for semiconductor devices and their applications [1,2]. This compound is relatively easy to prepare due to its high oxygen affinity and low temperature of melting of magnesium [3-5]. So many research works have been performed for the production and description of nonporous MgO either as powder or as thin films [6,7]. Much attempt has been devoted to the assembly of nanostructures of MgO using several techniques such as chemical spray pyrolysis [8], sol-gel [9,10], sonochemical [11], electron spinning [12], silar [13], and magnetron sputtering [14-17]. Amongst, the sol-gel method provides high-quality oxide materials that are easily adapted for thin film preparation [18,19]. The exceptionally smooth surface of films prepared using sol-gel method is crucial for achieving the appropriate characteristics in many applications [20,21]. Other benefits of this method contain great purity of the precursor, high homogeneity of the materials, low processing heat, no need for vacuum environment, low operation cost, and high resilience [22,23].

The aim of this search is to find, the influence of the doping of TiO_2 on the structure, optical, and sensing properties of MgO thin films by using sol-gel technique.

2. Experimental Details

In this paper, the route of the inorganic precursor was selected to fabricate MgO nano-doped with TiO_2 thin films. In the first step, MgO was prepared by dissolving 8.3 g Magnesium acetate tetrahydrate $(CH_3COO)_2Mg{\cdot}4H_2O$) (99%) in 30 ml of methanol. Nitric acid is added to the solution while stirring as a catalyst. The stirring was continued for 1 hour at room temperature to obtain a clear and homogeneous solution. In the second step, TiO_2 was prepared by using $Ti\{OCH(CH_3)_2\}_4$, the ethanol C_2H_5OHEtOH and acetic acid CH_3COOH as a catalyst, Obtained of all materials were from (Sigma Aldrich) with a purity of 99%. A gel solution was attained by dissolving 3.15 ml of TIP in 25 ml of ethanol and 5 ml of acetic acid, and for 1 hour was the solution stirred. In the third step, add TiO_2 to MgO solution with volume ratio (V/V) of 3% and 5% with stirred at 60°C for 30 minutes to obtain a homogenous MgO aqueous solution which leaves to 24 hours at room temperature before the deposition process. Then, Pure and TiO_2, doped MgO was deposited on quartz substrate using dip coating technique and then dried on a hot plate for 25 min at 100°C. Finally, the films were annealed with a furnace for 3 hours at 550°C to obtain nanocrystallization of MgO.

Structure crystal analysis of MgO films based on and using a SHIMADZU XRD system with CuKα1 irradiation with λ=1.54Å. The size of the crystal was calculated using the equation of Scherer [24]:

$$D = k\lambda / \beta \cos\theta \quad (1)$$

where k is a constant to be booked as 0.9, λ is the wavelength of x-ray (1.54 Å), β is the full-width at half maximum (FWHM), and θ is the diffraction or Bragg's angle of the XRD peak

Optical transmittance and absorbance measurements were performed using a SHIMADZU 1800 dual-beam UV/VISIBLE spectrophotometer in the wavelength range of 300-1000 nm.

3. Results and Discussion

Figure (1) shows the transmission spectra of pure and doped MgO films in the UV and visible regions of electromagnetic spectrum. The transmittance decreases with increasing doping level to be 63%, 55% and 52% for pure, 3 wt.% and 5 wt.% samples, respectively. This behavior is ascribed to the increase in the tuning of free electrons as the dopant (TiO_2) concentration is increased.

The absorption coefficient (α) of the prepared thin films was calculated from the following equation [25]:

$$\alpha = 2.303\ A/t \quad (2)$$

where A is the absorbance, and t is the film thickness

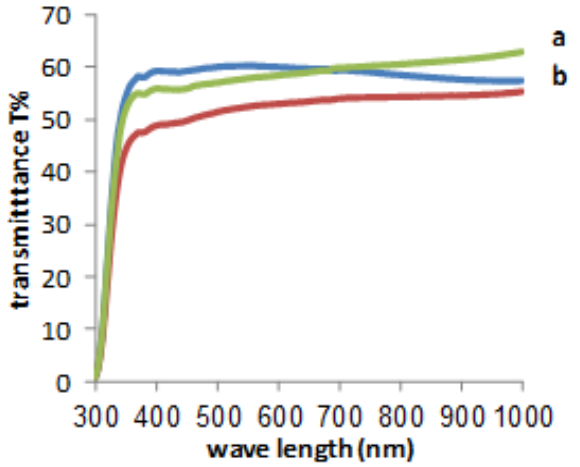

Fig. (1) Variation of transmittance with wavelength of MgO films for various doping of TiO_2 (a) pure, (b) 3%, and (c) 5%

The energy band gap of the prepared thin films are calculated from the following equation [26]:

$$\alpha h\nu = A(h\nu - E_g)^r \quad (3)$$

where h is Planck's constant, ν is the frequency of the incident light, E_g is the energy of the optical band gap of the material, r is a constant indicating the type of transition (direct or indirect, allowed or forbidden), A is a constant, $h\nu$ is the photon energy

Figure (2) represents the Tauc's relation to show the variation of $(\alpha h\nu)^2$ with the photon energy ($h\nu$). The results show that the energy band gap of the sample doped with 5 wt.% TiO_2 decreased from 4 to 3.68 eV, which means that the absorption edge was shifted from 310 to 336 nm. This decrease is due to the formation of donor sub-levels within the energy gap [27,28].

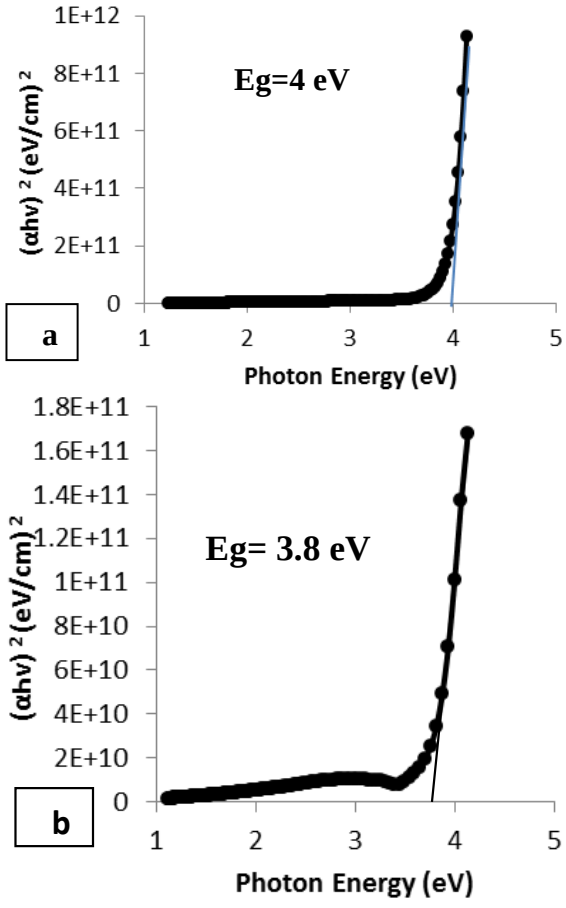

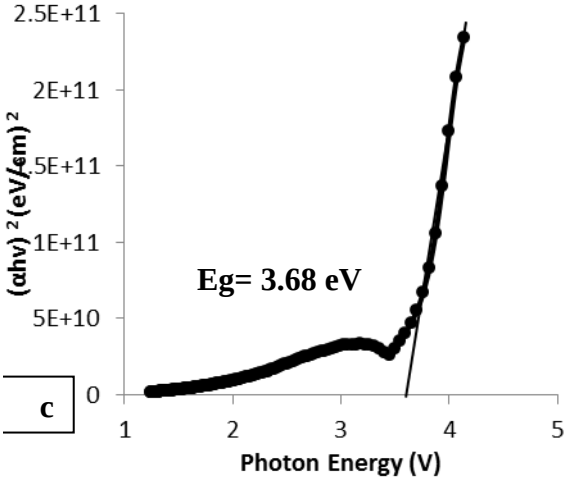

Fig. (2) Plots of $(\alpha hv)^2$ versus photon energy for MgO films for different doping of TiO_2 (a) pure, (b) 3%, and (c) 5%

4. Conclusion

In this work, pure and TiO_2-doped MgO thin films were prepared using sol-gel method. The optical properties of the prepared films were studied as functions of heat treatment. All samples showed high transmittance in the visible region, which decreases with increasing TiO_2 doping level. The values of the optical band gap are noticed to decrease from 4 to 3.68 eV at higher TiO_2 doping levels. The results of SEM and AFM display that the grain size decreases as the doping level is increased. The prepared films were then exposed to NH_3 gas to determine their sensitivity as gas sensors. The results show that the MgO thin films doped with 5 wt.% TiO_2 exhibit much more sensitivity to NH_3 gas than pure MgO films.

References

[1] A.O. Mousa, N.A. Nema and H.T. Saleem, "Study of structural and optical properties for MgO films prepared by using chemical spray pyrolysis technique", MSAIJ, 14(11) (2016) 426-434.

[2] N. Chaouch, S. Benramache and S. Lakel, "Synthesis and Characterization of Physical Properties of MgO Thin Films by Various Concentrations", *J. Microelectron. Electron. Pack.*, 17(1) (2020) 23-27.

[3] M. Fatehi, M. Ghasemifard and E. Fathi, "Determination of Optical Constants N and K for MgO Nanopowder Using Kramers-Kronig Equation", *Int. J. Eng. Res. Technol.*, 8(3) (2014) 330-334.

[4] M.A. Hameed, S.H. Faisal, R.H. Turki, "Characterization of Multilayer Highly-Pure Metal Oxide Structures Prepared by DC Reactive Magnetron Sputtering Technique", *Iraqi J. Appl. Phys.*, 16(4) (2020) 25-30

[5] M. Ikram et al., "Graphene Oxide-Doped MgO Nanostructures for Highly Efficient Dye Degradation and Bactericidal Action", *Nanoscale Res. Lett.*, 16(56) (2021) 1-11.

[6] J.Y. Kim, H.S. Jung and K.S. Hong, "Effects of Acetic Acid on the Crystallization Temperature of Sol–Gel-Derived MgO Nano-Powders and Thin Films", *J. Am. Cer. Soc.*, 88(3) (2005) 784-787.

[7] H. Güney and D. Iskenderoglu, "Characterization of MgO:Cd thin films grown by SILAR method", *Can. J. Phys.*, 96 (2018) 804-809.

[8] O.V. Diachenko et al., "Surface Morphology, Structural and Optical Properties of MgO Films Obtained by Spray Pyrolysis Technique", *Acta Phys. Pol. A*, 3(130) (2016) 805-810.

[9] M.S. Wagh et al., "Preparation of MgO Nanostructure Powder by Sol-gel Method", Int. J. Chem. Phys. Sci., 4 (2015) 115-117.

[10] S. Suresh, "Investigations on Synthesis, Structural and Electrical Properties of MgO Nanoparticles by Sol-Gel Method", *J. Ovonic Res.*, 6(10) (2014) 205-210.

[11] A. Alavi and A. Morsali, "Syntheses and characterization of $Mg(OH)_2$ and MgO nanostructures by ultrasonic method", *Ultrason. Sonochem.*, 17 (2010) 441-446.

[12] R. Murugan et al., "Magnesium oxide nanotubes: synthesis, characterization and application as efficient recyclable catalyst for pyrazolyl1,4-dihydropyridine derivatives", *Tetrahedron*, 35(68) (2012) 7196-7201.

[13] Y. Akaltun et al., "The effect of wettability on corrosion resistance of oxide films produced by SILAR method on magnesium, aluminum and copper substrates", *Surf. Coat. Technol.*, 292 (2016) 121-131.

[14] F.J. Al-Maliki et al., "Enhanced photocatalytic activity of Ag-doped TiO_2 nanoparticles synthesized by DC Reactive Magnetron Co-Sputtering Technique", *Opt. Quantum Electron.*, 52 (2020) 188.

[15] R.H. Turki and M.A. Hameed, "Spectral and Electrical Characteristics of Nanostructured NiO/TiO_2 Heterojunction Fabricated by DC Reactive Magnetron Sputtering", *Iraqi J. Appl. Phys.*, 16(3) (2020) 39-42.

[16] R.A.H. Hassan and F.T. Ibrahim, "Preparation and Characterization of Ni-doped TiO_2 Nanostructures for Surface Cleaning Applications", *Iraqi J. Appl. Phys.*, 17(1) (2021) 3-8.

[17] Z. Mohammed, S. Khalil and M. Mutter, "Synthesis and characterization of ZrO_2:MgO thin films by plasma of R.F. magnetron sputtering", *Karbala Int. J. Mod. Sci.*, 1(5) (2019) 11-18.

[18] F.T. Ibrahim, "Characterization of Pulsed-Laser Deposited CuO-Doped MgO Thin Films for Gas Sensing Applications", *Iraqi J. Appl. Phys.*, 3(13) (2017) 13-17.

[19] M.S. Mastuli et al., "Effects of Lithium Dopant on Size and Morphology of Magnesium Oxide Nanopowders", *Malaysian J. Anal. Sci.*, 1(18) (2014) 15-20.

[20] S. Bais and R.K. Pathak, "Corrosion and Structural studies of Galvanostatically Electrodeposited ZnMgO Thin Films", Int. J. Sci. Res., (2015) 1163-1168.

[21] B.G. Obeid, A.S. Hameed and H.H. Alaaraji, "Structural and Optical Properties of TiO_2:MgO Thin Films Preparing at 373K", *Digest J. Nanomater. Biostruct.*, 4(12) (2017) 1239-1246.

[22] T. Serin et al., "Electrical, structural and optical properties of SnO_2 thin films prepared by spray pyrolysis", *J. Noncryst. Solids*, 352(3) (2006) 209-215.

[23] H. Shokry Hassan et al., "Synthesis, Characterization and Fabrication of Gas Sensor Devices Using ZnO and ZnO:In Nanomaterials", *Beni-Suef Univ. J. Basic Appl. Sci.*, 4(4) (2014) 1-6.

[24] A. Patterson, "The Scherrer formula for X-Ray particle size determination", *Phys. Rev.*, 56(10) (1939) 978-982.

[25] F.J. Kadhim, O.A. Hammadi and N.H. Mutesher, "Photocatalytic activity of TiO_2/SiO_2 nanocomposites synthesized by reactive magnetron sputtering technique", *J. Nanophot.*, 16(2) (2022) 026005 DOI: 10.1117/1.JNP.16.026005.

[26] J. Tauc, "Optical properties and electronic structure of amorphous Ge and Si", *Mater. Res. Bull.*, 3(1) (1968) 37-46.

[27] E.A. Al-Oubidy and F.J. Al-Maliki, "Effect of Gas Mixing Ratio on Energy Band Gap of Mixed-Phase Titanium Dioxide Nanostructures Prepared by Reactive Magnetron Sputtering Technique", *Iraqi J. Appl. Phys.*, 14(4) (2018) 19-23.

[28] O.A. Hammadi, F.J. Kadhim and E.A. Al-Oubidy, "Photocatalytic Activity of Nitrogen-Doped Titanium Dioxide Nanostructures Synthesized by DC Reactive Magnetron Sputtering Technique", *Nonl. Opt. Quantum Opt.*, 51(1-2) (2019) 67-78.

Sensing Properties of Nanocrystalline MgO:TiO_2 Thin Films Prepared by Sol-Gel Method

Amel S. Suber, Hanaa K. Khalaf, Seham Z. Abbas, Mohammed E. Ismael

Directorate of Materials Research, Ministry of Science and Technology, Baghdad, IRAQ

Abstract

In this paper, the sensing properties of nanocrystalline MgO and MgO:TiO_2 films deposited on quartz substrates by sol-gel method are studied. The films were heated in air at 550 °C for 3 hours. The films were examined for their ability to sense NH_3 gas at 6 ppm at room temperature by measuring their sensitivity to this gas at various times. Our results demonstrated that the films were very highly sensitive to NH_3 gas, and the design and fabrication of the ammonia detection gas sensor at room temperature.

Keywords: Thin films; Sol-gel; magnesium oxide; Titanium dioxide; Gas sensors
Received: 4 May 2022; **Revised:** 6 July 2022; **Accepted:** 13 July 2022; **Published:** 1 October 2022

1. Introduction

Metal oxides are very important materials of technology for use in electronics and devices of photonic [1]. Magnesium oxide (MgO) is a very convenient filter for applications of insulation owing to its low capacity of heat and high melting point [2-4], pollutant absorbents [5], and gas sensor [6]. Nowadays, the use of MgO and its devices might be more intriguing due to their potential use as heterogeneous catalysts and supports for metal nanoparticles in electronic devices, insulating metal oxides have received a lot of attention recently [7-10].

The aim of this search is to find, the influence of the doping of TiO_2 on the structure, optical, and sensing properties of MgO thin films by using sol-gel technique.

2. Experimental Details

In this paper, the route of the inorganic precursor was selected to fabricate MgO nano-doped with TiO_2 thin films. In the first step, MgO was prepared by dissolving 8.3 g magnesium acetate tetrahydrate $(CH_3COO)_2Mg{\cdot}4H_2O$) (99%) in 30 ml of methanol. Nitric acid is added to the solution while stirring as a catalyst. The stirring was continued for 1 hour at room temperature to obtain a clear and homogeneous solution. In the second step, TiO_2 was prepared by using $Ti\{OCH(CH_3)_2\}_4$, the ethanol C_2H_5OHEtOH and acetic acid CH_3COOH as a catalyst, Obtained of all materials were from (Sigma Aldrich) with a purity of 99%. A gel solution was attained by dissolving 3.15 ml of TIP in 25 ml of ethanol and 5 ml of acetic acid, and for 1 hour was the solution stirred. In the third step, add TiO_2 to MgO solution with volume ratio (V/V) of 3% and 5% with stirred at 60°C for 30 minutes to obtain a homogenous MgO aqueous solution which leaves to 24 hours at room temperature before the deposition process. Then, Pure and TiO_2, doped MgO was deposited on quartz substrate using dip coating technique and then dried on a hot plate for 25 min at 100°C. Finally, the films were annealed with a furnace for 3 hours at 550°C to obtain nanocrystallization of MgO.

Structure crystal analysis of MgO films based on and using a SHIMADZU XRD system with CuKα1 irradiation with λ=1.54Å. The size of the crystal was calculated using the equation of Scherer [11]:

$$D = k\lambda / \beta \cos\theta \quad (1)$$

where k is a constant to be booked as 0.9, λ is the wavelength of x-ray (1.54 Å), β is the full-width at half maximum (FWHM), and θ is the diffraction or Bragg's angle of the XRD peak

The shapes of the resulting films were described by a CSPM- 5000 atomic force microscope (AFM).

3. Results and Discussion

Figure (1) displays the diffraction of x-ray diffraction patterns of TiO_2-doped MgO films

at different concentrations of TiO_2 doping (pure, 3, and 5 wt.%), on quartz substrates annealed at 550°C. The XRD patterns reveal strong and sharp (200) and (220) diffraction peaks respectively indicating the formation of MgO. All films are polycrystalline with a cubic structure. The TiO_2-phase compound at these peaks could not be confirmed by XRD due to small levels of TiO_2 doping. The crystallite size was calculated using Eq. (1) to be 35.2, 22.4 and 12.2 nm for doping levels of 0, 3, and 5 wt.%. of TiO_2 doping, respectively. It is clear that the crystallite size decreases with the TiO_2 doping level due to the difference in molecular size between MgO and TiO_2, which can cause a slight lattice disruption and these results are in agreement with [12-14].

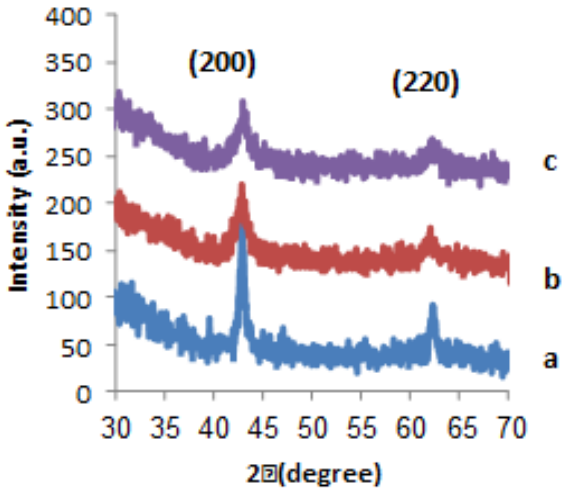

Fig. (1) XRD patterns of MgO films at different doping levels of TiO_2 (a) pure, (b) 3%, and (c) 5%

Figure (2) reveals the 3D AFM profiles of pure and doped MgO thin films for different concentrations of TiO_2 (pure, 3 and 5 wt.%). The regular size of the grain of the doped and pure MgO films is measured from AFM results using software to be 90-60nm. The AFM results show that by the TiO_2-doped MgO thin films were rougher than the pure film, and the grain size became smaller. This result is consistent with [21].

The sensitivity (S%%) of the MgO thin film gas sensor is usually defined as the ratio of the film surface resistance (R_a) in air to that in presence of gas (R_g) as [15]

$$S = \left|\frac{R_g - R_a}{R_a}\right| \times 100 \qquad (4)$$

The sensitivity of MgO thin film for NH_3 gas has been studied at a concentration of 6 ppm. The sensitivity of MgO thin films prepared by dip coating on quartz substrates with different concentrations of TiO2 as a function of operating time for NH_3 gas with operation temperatures at room temperature is shown in Fig. (3). The sensitivity increases with operating time for all films. The sensitivity of the semiconducting metal oxide sensor is determined by the reaction between the gas and the film sensor surface.

Fig. (2) 3D AFM images of MgO films at various concentrations of doping with TiO_2 (a) pure, (b) 3%, and (c) 5%

It is noticed that the sensitivity for all samples increases with increasing the concentration of TiO_2 doping. The sensitivity of pure MgO film is lower than that of doped MgO films and the MgO film doped with 5wt.% TiO_2 has the highest sensitivity at room temperature. The decrease in the sensitivity, in this case, is due to the effect of the change in the grain size [16-18]. Sensor samples with

small particles and high roughness have high surface area, which provides more active sites where invasive species absorb and interact. The sensitivity of pure MgO and TiO_2-doped MgO thin films to NH_3 at room temperature for all samples is illustrate in table (1).

Table (1) Values of sensitivity (S) for pure MgO and MgO:TiO_2 for NH_3 gas

Gases	TiO_2 doping concentrations	Sensitivity (S)% at R.T
NH_3	pure	11
	3%	27
	5%	40

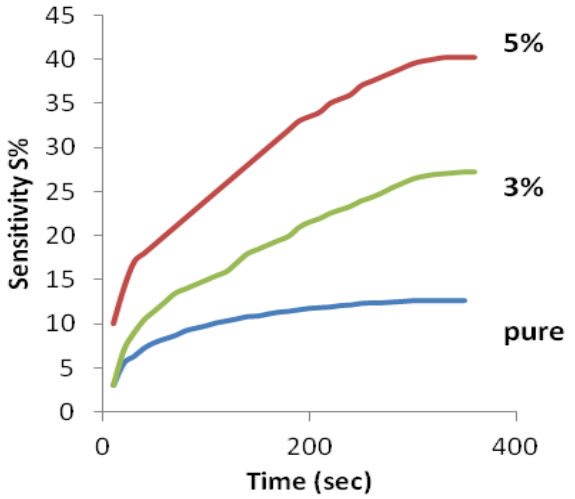

Fig. (3) Sensitivity (S%) as a function of time for MgO films of different doping concentrations of TiO_2

Figure (4) shows the variation of sensitivity to NH_3 gas with operating temperature for pure and TiO_2-doped MgO films annealed at 550°C. The sensitivity increases with increasing TiO_2 doping level for all films. This figure also shows that the sensitivity increases with increasing operating temperature to reach its maximum corresponding to an optimum operating temperature (250°C) as the resistance drops and the sensitivity rises. Furthermore, the sensitivity to NH_3 gas drops at 300°C as the higher operating temperature makes the lifetime of electrons in the sensor device shorter and increases the resistance, thus, the sensor is requiring excess electrons to operate [19,20].

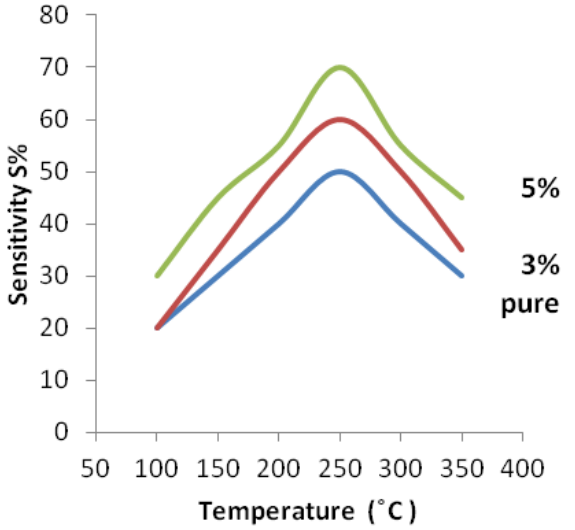

Fig. (4) Sensitivity (S%) as a function of temperature plot of MgO films for various doping concentrations of TiO_2 for NH_3 gas

4. Conclusion

In this work, pure and TiO_2-doped MgO thin films were prepared using sol-gel method. The structural properties of the prepared films were studied as functions of heat treatment. Structural characterization showed that all films are polycrystalline and the degree of crystallinity decreases with increasing TiO_2 doping level. The prepared films were then exposed to NH_3 gas to determine their sensitivity as gas sensors. The results show that the MgO thin films doped with 5 wt.% TiO_2 exhibit much more sensitivity to NH_3 gas than pure MgO films.

References

[1] A.O. Mousa, N.A. Nema and H.T. Saleem, "Study of structural and optical properties for MgO films prepared by using chemical spray pyrolysis technique", MSAIJ, 14(11) (2016) 426-434.

[2] N. Chaouch, S. Benramache and S. Lakel, "Synthesis and Characterization of Physical Properties of MgO Thin Films by Various Concentrations", *J. Microelectron. Electron. Pack.*, 17(1) (2020) 23-27.

[3] M. Fatehi, M. Ghasemifard and E. Fathi, "Determination of Optical Constants N and K for MgO Nanopowder Using Kramers-Kronig Equation", *Int. J. Eng. Res. Technol.*, 8(3) (2014) 330-334.

[4] M.A. Hameed, S.H. Faisal, R.H. Turki, "Characterization of Multilayer Highly-Pure Metal Oxide Structures Prepared by DC Reactive Magnetron Sputtering Technique", *Iraqi J. Appl. Phys.*, 16(4) (2020) 25-30

[5] M. Ikram et al., "Graphene Oxide-Doped MgO Nanostructures for Highly Efficient Dye Degradation and Bactericidal Action", *Nanoscale Res. Lett.*, 16(56) (2021) 1-11.
[6] J.Y. Kim, H.S. Jung and K.S. Hong, "Effects of Acetic Acid on the Crystallization Temperature of Sol–Gel-Derived MgO Nano-Powders and Thin Films", *J. Am. Cer. Soc.*, 88(3) (2005) 784-787.
[7] H. Güney and D. Iskenderoglu, "Characterization of MgO:Cd thin films grown by SILAR method", *Can. J. Phys.*, 96 (2018) 804-809.
[8] O.V. Diachenko et al., "Surface Morphology, Structural and Optical Properties of MgO Films Obtained by Spray Pyrolysis Technique", *Acta Phys. Pol. A*, 3(130) (2016) 805-810.
[9] M.S. Wagh et al., "Preparation of MgO Nanostructure Powder by Sol-gel Method", Int. J. Chem. Phys. Sci., 4 (2015) 115-117.
[10] S. Suresh, "Investigations on Synthesis, Structural and Electrical Properties of MgO Nanoparticles by Sol-Gel Method", *J. Ovonic Res.*, 6(10) (2014) 205-210.
[11] A. Alavi and A. Morsali, "Syntheses and characterization of $Mg(OH)_2$ and MgO nanostructures by ultrasonic method", *Ultrason. Sonochem.*, 17 (2010) 441-446.
[12] R. Murugan et al., "Magnesium oxide nanotubes: synthesis, characterization and application as efficient recyclable catalyst for pyrazolyl1,4-dihydropyridine derivatives", *Tetrahedron*, 35(68) (2012) 7196-7201.
[13] Y. Akaltun et al., "The effect of wettability on corrosion resistance of oxide films produced by SILAR method on magnesium, aluminum and copper substrates", *Surf. Coat. Technol.*, 292 (2016) 121-131.
[14] F.J. Al-Maliki et al., "Enhanced photocatalytic activity of Ag-doped TiO_2 nanoparticles synthesized by DC Reactive Magnetron Co-Sputtering Technique", *Opt. Quantum Electron.*, 52 (2020) 188.
[15] M.S. Mastuli et al., "Effects of Lithium Dopant on Size and Morphology of Magnesium Oxide Nanopowders", *Malaysian J. Anal. Sci.*, 1(18)
[16] B.G. Obeid, A.S. Hameed and H.H. Alaaraji, "Structural and Optical Properties of TiO_2:MgO Thin Films Preparing at 373K", *Digest J. Nanomater. Biostruct.*, 4(12) (2017) 1239-1246.
[17] T. Serin et al., "Electrical, structural and optical properties of SnO_2 thin films prepared by spray pyrolysis", *J. Noncryst. Solids*, 352(3) (2006) 209-215.
[18] H. Shokry Hassan et al., "Synthesis, Characterization and Fabrication of Gas Sensor Devices Using ZnO and ZnO:In Nanomaterials", *Beni-Suef Univ. J. Basic Appl. Sci.*, 4(4) (2014) 1-6.
[19] A. Patterson, "The Scherrer formula for X-Ray particle size determination", *Phys. Rev.*, 56(10) (1939) 978-982.
[20] F.J. Kadhim, O.A. Hammadi and N.H. Mutesher, "Photocatalytic activity of TiO_2/SiO_2 nanocomposites synthesized by reactive magnetron sputtering technique", *J. Nanophot.*, 16(2) (2022) 026005 DOI: 10.1117/1.JNP.16.026005.
[21] E.A. Al-Oubidy and F.J. Al-Maliki, "Effect of Gas Mixing Ratio on Energy Band Gap of Mixed-Phase Titanium Dioxide Nanostructures Prepared by Reactive Magnetron Sputtering Technique", *Iraqi J. Appl. Phys.*, 14(4) (2018) 19-23.

Effects of Defect Concentration and Work Gunctio on Performance of Pervoskite-Based Solar Cells

Dhuha E. Tareq, Fouad A. Senaed, Ahmad. A. F.

Alayen University, Nasiriyah, IRAQ

Abstract
In this work, a planar heterojunction perovskite-based solar cell's conventional structure consisting of a back electrode, hole transport material (HTM), perovskite absorber, electron transport material (ETM), and transparent electrode is proposed. This study used ETM (SnO_2) with the perovskite $CH_3NH_3PbBr_3$ and found that the combination of SnO_2 and perovskite produced a high efficiency. Device performance has been shown to be significantly impacted by the HTM's hole mobility and acceptor concentration, interface trap density, and back contact metal's work-function.

Keywords: Tin dioxide; Solar cells; Perovskite solar cells; Organometal halides; Electron transport material
Received: 5 May 2022; **Revised:** 7 July 2022; **Accepted:** 14 July 2022; **Published:** 1 October 2022

1. Introduction

The most significant factor The solar photovoltaic cell design attempts to maximize cost-effectiveness ratio, which entails reducing the overall cost while enhancing the longevity and performance of PV module [1-5]. Numerous factors can impact an efficiency of solar cell. First and most vital component is how much electromagnetic energy passes through the absorber layer and is used by the solar cell to produce energy. Second, various materials' coefficients of absorption, band gaps, and consequently theoretical maximum efficiencies vary [6]. The former's thickness could not be ideal for the deployment of charge carriers, whilst the latter's intensity rises and output falls [7]. The amount of light that is absorbed by the substance, or the amount of light that reaches the substance that is absorbing, reflecting, transmitting, and absorbing light is the fifth factor. The sixth factor that has an impact on efficiency is temperature sensitivity [8].

In structures of perovskite with the general formula ABX_3 (X is carbon, oxygen, nitrogen, or halogen), the cation is filled on a cubooctahedral site, while the B cation is occupied on an octahedral site (Fig. 1). When used with O_2 anion, the elements A and B are frequently divalent and tetravalent. On the other hand, monovalent and divalent cations can be used at sites A and B when perovskites containing halogen anions are present. The A-site cation in $CH_3NH_3PbI_3$ is $CH_3NH_3^+$, and the B-site cation is Pb^{2+}, as shown in (Fig. 2b). The formability of perovskite is determined using the geometric tolerance factor (t) [7,9], $t = (r_A+r_X)/[H_2(r_B+r_X)]$, where the effective ionic radii for ions A, B, and X are, respectively, r_A, r_B, and r_X. A perfect cubic perovskite is anticipated for transition metal cations that make up oxide perovskite when t=1, however an octahedral distortion is observed at t=1 [8,10].

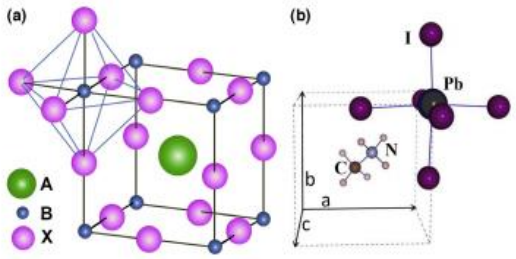

Fig. (1) (a) the structure of the perovskite ABX3 with the larger A cation occupied in the Cubo octahedral position and the BX6 octahedral structure. (b)show A cubic perovskite unit cell made of $CH_3NH_3PbI_3$. The first image in (b) was lifted from Ref. [9]

Burgelman et al. have developed the SCAPS 1D simulator by solving basic semiconductor device equations in a stable environment [10] to thin film heterojunction solar cells' electrical properties in a model. It was used in this study to examine how a real

solar cell ($MASnI_3$) device performed with various material parameters. Both interface defect recombination and deep bulk level defect recombination are supported by the program (non-radiative recombination) [11]. Radiative (direct band-to-band recombination) and interface recombination account for a sizable portion of the system's recombination losses, which are counterbalanced by Shockley-Read-Hall recombination (propagated by defects or traps) [12]. The flow chart below shows the steps involved in SCAPS simulation.

Radiative recombination (direct band-to-band recombination) and interface recombination account for a sizable portion of the recombination losses in the system under consideration, which are balanced by Shockley-Read-Hall recombination (propagated by defects or traps). Figure (2) shows a flow chart of the SCAPS simulation's stages in detail [11,12].

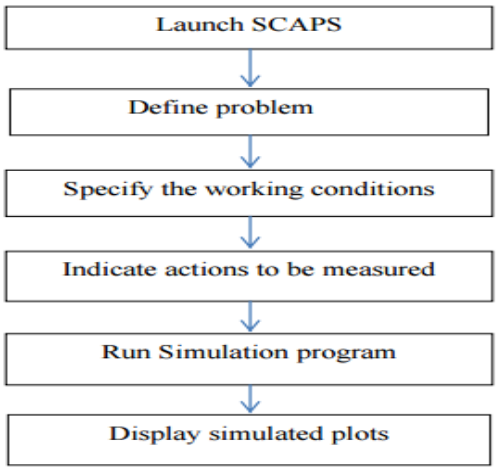

Fig. (2) Simulation procedure

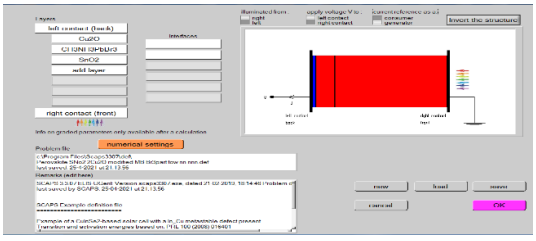

Fig. (3) Heterojunction solar cells made of $C_2uO/CH_3NH_3PbI_3/TiO_2$, $C_2uO/CH_3NH_3PbBr_3/ZnO$ on a SCAPS panel

It's important to note that the simulation parameters for the architecture's layers were selected with consideration for existing experimental results and relevant research [14]. The main variables of the simulation are listed in table (1).

Table (2) The ETM composition , the absorber, and the HTM [15-16]

Parameters	Cu_2O	$CH_3NH_3PbBr_3$	SnO_2
Band gap (ev)	2.17	2.33 [18]	3.5
Effinity of Electron (ev)	3.20	3.70 [19]	4
Electrical conductivity	7.11	7.50 [21]	9
CB state-effective density ($1/cm^2$)	2.02E+17	1.00+17 [21]	4.300E+18
VB state-effective density ($1/cm^2$)	1.10E+19	1.00+17 [21	2.500E+19
Mobility of electron ($cm^2/v.s$)	2.000E+2	24 [22]	1.000E+7
mobility of hole ($cm^2/v.s$)	8.00E+18	24 [22]	1.000E+7

2. Discussion

The variation of solar cell properties as a defect function density as shown in Fig. (4). The simulation model's flaw density ranges from $2x10^{17}$ to $14x10^{17}$ cm^{-3}. With increasing flaw density, the PV parameters randomly decrease. The lowest defect density in the absorber layer is $2x10^{17}$ cm^{-3}, and the highest PV attributes are an efficiency of 40.61%, a fill factor of 64.31%, a J_{SC} of 46.01 mA/cm^2, and a V_{OC} of 1.37 V. This makes it obvious that cells perform considerably worse when the defect concentration is increased [17-19].

Simulations have employed a variety of metals as potential back contacts for perovskite solar cells, including silver (Ag), iron (Fe), copper (Cu), graphite alloy, gold (Au), nickel (Ni), cr, si, and platinum (Pt). The majority carrier barrier height (relative to Ef) decreases as metal work function rises as a result of band bending at the metal-semiconductor interface, increasing the contact's ohmicity. Every parameter increases in line with the increase in the metal's work function.

Table (3) Device parameters and defect for $Cu_2O/CH_3NH_3PbBr_3/SnO_2$

Defect Nt($1/cm^3$)	Voc (volt)	Jsc (mA/cm^2)	FF	Efficiency%
$2*10^{17}$	1.37	46.01	64.31	40.61
$4*10^{17}$	1.36	45.89	64.28	40.41
$6*10^{17}$	1.36	45.78	64.25	40.24
$8*10^{17}$	1.36	45.68	64.23	40.09
$10*10^{17}$	1.36	45.58	64.21	39.96
$12*10^{17}$	1.36	45.49	64.20	39.85
$14*10^{17}$	1.36	45.41	64.20	39.75

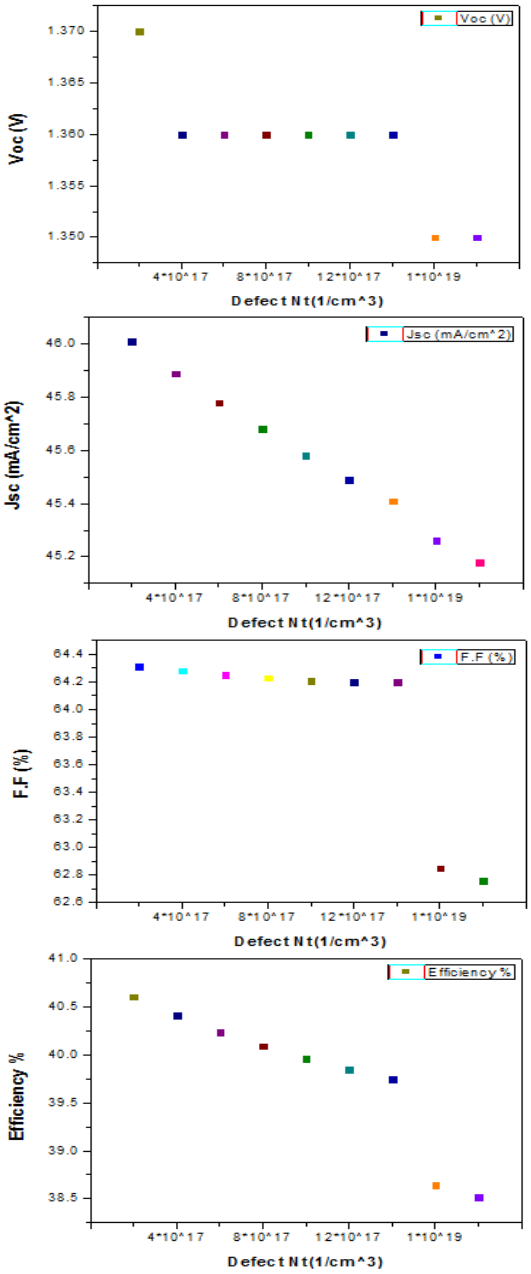

Fig. (4) Solar cell parameters as functions of defect concentration in the HTM/$CH_3NH_3PbBr_3$/ETM layer

Table (4) Impact of different metal contacts on the cell's efficiency

Work Function(ev)	Voc (volt)	Jsc (mA/cm^2)	FF	Efficiency %
Cr	4.5	0.9	45.64	15.71
Si	4.6	1.08	45.73	19.75
Ag	4.7	1.22	45.8	23.87
Ta	4.8	1.15	45.86	28.06
Zn	4.9	1.08	45.92	32.3
Co	5	1.1	45.97	36.56
Au	5.1	1.3	46.01	40.61
Pt	5.12	`1.48	46.02	41.23

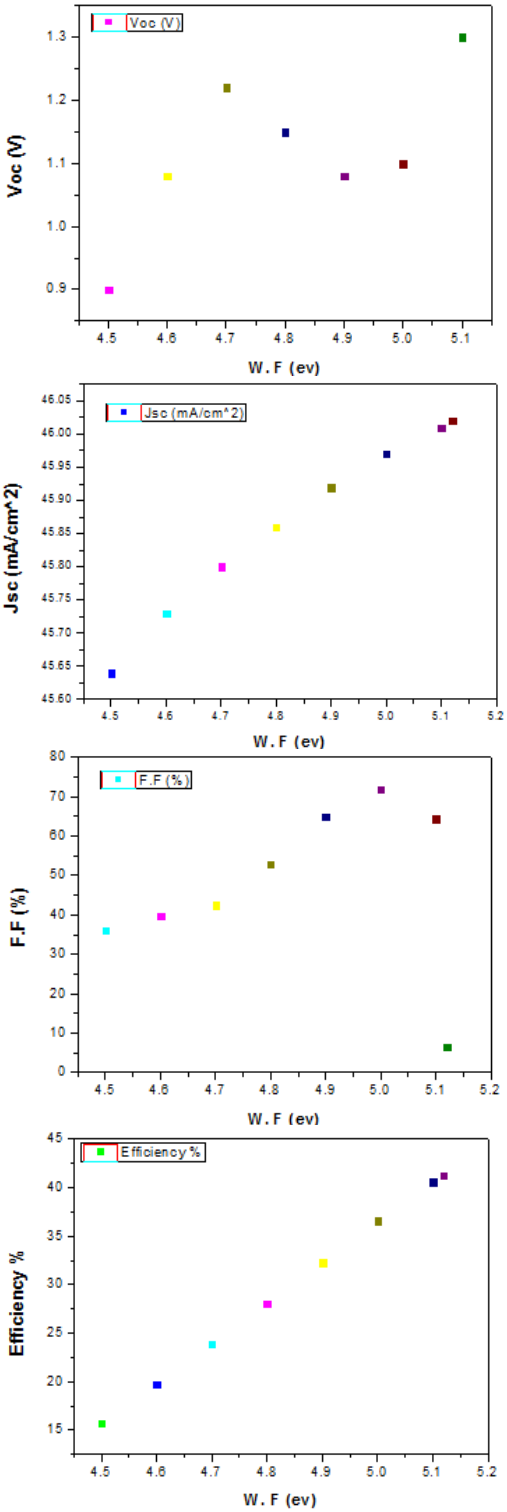

Fig. (5) Solar cell parameter as functions of the metal work function

3. Conclusions

In this study, a change in $CH_3NH_3PbBr_3$, SnO_2 thickness was noted. The study also investigated a wide range of temperature, defect, and work function to identify the ideal parameters that matched to the

$Cu_2O/CH_3NH_3PbBr_3/SnO_2$ device's greatest efficiency, which achieved 41.23% at work function 5.12 eV.

References

[1] Y. Wang et al., "Solvent annealing of PbI2 for the high-quality crystallization of perovskite filmsfor solar cells with efficiencies exceeding 18%", *Nanoscale*, 8 (2016) 19654-19661.

[2] M.A. Green et al., "Solar cell efficiency tables (Version 47)", *Prog. Photovolt. Res. Appl.*, 24 (2016) 3-11.

[3] M.J. Taghavi et al., "Modeling of optical losses in perovskite solar cells", *Superlatt. Microst.*, 97 (2016) 424-428.

[4] A. Zhang, Y. Chen and J. Yan., "Optimal Design and Simulation of HighPerformance Organic-Metal Halide Perovskite Solar Cells", *IEEE J. Quantum. Electron.*, 52(6) (2016) 1-6.

[5] D. Bottaro and J. Moscowitz, "Current photovoltaic technology: current progress and future prospects", MIT Energy Lab. Rep.- MIT-EL 77-041W (1977).

[6] W. Shockley and H.J. Queisser, "Detailed balance limit of efficiency of pn junction solar cells", *J. Appl. Phys.*, 31 (1961) 510-519.

[7] V.M. Goldschmidt, "Crystal structure and chemical composition", Ber. Dtsch. Chem. Ges. 60 (1927) 1263–1268.

[8] M. Rini et al., "Control of the electronic phase of a manganite by mode-selective vibrational excitation", *Nature*, 449 (2007) 72-74.

[9] G. Giorgi et al., "Small Photocarrier Effective Masses Featuring Ambipolar Transport in Methylammonium Lead Iodide Perovskite: A Density Functional Analysis", *J. Phys. Chem. Lett.*, 4 (2013) 4213–4216.

[10] M. Burgelman et al, SCAPS manual, no. May. 2014.

[11] A. Niemegeers, M. Burgelman and K. Decock, SCAPS Manual, University of Gent (2014).

[12] T. Minemoto and M. Murata, "Device modeling of perovskite solar cells based on structur- al similarity with thin film inorganic semiconductor solar cells", J. Appl. Phys., 116(5) (2014) 054505.

[13] T.L. Amu, "Performance Optimization Of Tin Halide Perovskite Solar Cells Via Numerical Simulation", Ph.D. thesis, University of Abuja (Nigeria) (2014).

[14] M.I. Hossain et al., "Design optimization of solar cell with molybdenum sulfide as light absorber", *J. Photon. Ener.*, 8(2) (2018) 025501.

[15] C. Wehrenfennig, "Ultrafast spectroscopy of charge separation, transport and recombination processes in functional materials for thin-film photovoltaics", Ph.D. thesis, Oxford University (2014).

[16] M. Nawaz, E.S. Marstein and A. Holt, "Design analysis ZnO/cSi heterojunction solar cell", in Proc. IEEE Photovol. Special. Conf. (PVSC) Honolulu, 20–25 June (2010) 2213–2218.

[17] O.A. Hamadi, B.A.M. Bader and A.K. Yousif, "Electrical Characteristics of Silicon p-n Junction Solar Cells Produced by Plasma-Assisted Matrix Etching Technique", *Eng. Technol. J.*, 28 (2008).

[18] S.H. Faisal and M.A. Hameed, "Heterojunction Solar Cell Based on Highly-Pure Nanopowders Prepared by DC Reactive Magnetron Sputtering", *Iraqi J. Appl. Phys.*, 16(3) (2020) 27-32.

[19] O.A. Hammadi and N.E. Naji, "Effect of Acidic Environment on the Spectral Properties of Hibiscus sabdariffa Organic Dye used in Dye-Sensitized Solar Cells", *Iraqi J. Appl. Phys.*, 10(2) (2014) 27-31.

Table (1) The fundamental device equations [13]

Poisson equation	$\frac{\partial}{\partial x}(-\varepsilon(x)\frac{d\phi}{dx}) = q\left[p(x) - n(x) + N_D^+ - N_A^- + P_t(x) - n_t(x)\right]$
Continuity Equation for electrons	$\frac{\partial n(x,t)}{\partial t} = \frac{1}{q}\frac{\partial J_n}{\partial x} + G_n(x,t) - R_n(x,t)$
Continuity Equation for holes	$\frac{\partial p(x,t)}{\partial t} = \frac{1}{q}\frac{\partial J_p}{\partial x} + G_p(x,t) - R_p(x,t)$
Current density equation for electron	$J_p = q(p\mu_p E - D_p\frac{dp}{dx})$
Current density equation for holes	$J_p = q(p\mu_p E - D_p\frac{dp}{dx})$

XRD and FTIR Characterization of Carboxymethyl Cellulose Nanoparticles Synthesized from Plant Byproducts

Kadhim H. Abdul Sayed, Alaa G. Al-Hasimi, Kareema M. Ziadan

Department of Food Science, College of Agriculture, University of Basrah
Department of Physics, College of Science, University of Basrah

Abstract
In this study, the cellulose (C) was extracted from plant wastes such as rice husk and the preparation of nano-cellulose (NC) using acid hydrolysis and ultrasound method, and the preparation of carboxymethyl cellulose (CMC) and carboxymethyl nano cellulose (NCMC) by alkalization and etherification method were presented. Some characteristics of these compounds were studied, including the size of the natural polymers, the percentage of yield of nanopolymers, the functional groups using FT-IR spectroscopy, the structure using XRD patterns. It was found that the viscosity of nanopolymers decreased compared to polymers in the natural size, and it was 80.33 and 52.23 for CMC and NCMC, water binding capacity (WBC) recorded a decrease for the nanopolymers compared to the polymers in the natural size and it was 725.42% and 540.76% for CMC and NCMC, respectively, and the fat binding capacity (FBC) was 511.35% and 230.25% for CMC and NCMC, respectively.

Keywords: Polymers; Nanocellulose; Carboxymethyl cellulose; Nanoparticles; Toxicity
Received: 6 May 2022; **Revised:** 10 July 2022; **Accepted:** 17 July 2022; **Published:** 1 October 2022

1. Introduction

Biopolymers are biodegradable polymeric materials and include natural polymers of plant, animal and microbial origin or polymers are chemically manufactured from natural units such as polylactic acid [1]. Cellulose $(C_6H_{10}O_5)n$ is one of the most abundant biopolymers available in nature and is a major component of the cell wall [2]. Also, it is from homogeneous polymers formed by linking glucose units together with linkages from type (β,1-4) [3]. Moreover, each unit of cellulose contains three hydroxyl groups that can form hydrogen bonds, which makes cellulose unstable, poorly soluble in water, and poorly soluble in organic solvents [4]. Cellulose is a water-insoluble polymer because of its high crystallization degree and increased hydrogen bonds between polymer chains, which limits its uses in many food industries [5]. In order to overcome these problems, it is resorted to converting Cellulose to its water-soluble derivatives and common solvents, as these derivatives obtained through chemical reactions include Carboxymethyl cellulose (CMC), Methyl cellulose (MC), Hydroxypropyl cellulose (HPC), and Hydroxypropyl methylcellulose (HPMC) [6]. CMC is one of the most important straight chain anionic polysaccharides, which is a cellulose ether produced by replacing the hydroxyl groups in the glucose molecule of cellulose with a carboxymethyl group ($-CH_2$-COOH). CMC is prepared from the reaction of cellulose with sodium hydroxide (NaOH) and chloroacetic acid (monochloroacetic acid (MCA)) [7].

The study aimed to produce Carboxymethyl cellulose nanoparticles from the most abundant polymers in nature from agricultural food wastes, which constitute great harm and an increase in environmental pollution harmful to health. As well as studying the properties of these nanopolymer in terms of effective groups using FTIR, and their degree of crystallinity using XRD.

2. Materials and Methods

Rice husks were obtained from the local mill in Basra Governorate, sulfuric acid 98%, NaOH, $NaOCI_2$, acetone, ethanol, acetic acid, toluene, isopropanol, monochloroacetic, and laboratory materials from Sikma Company.

Nanocellulose was prepared from 10g of dried cellulose was weighed in a beaker containing 90 ml of 47% sulfuric acid (9 ml of acid/g of cellulose) and heated to 45°C with stirring with a magnetic stirrer (600 rpm) for 90 minutes. The reaction was stopped by adding 10 times cold distilled water, then centrifugation was carried out at 8000 rpm for 15 minutes at a temperature of 10°C. The centrifugation process was repeated until the pH reached neutral. After that, the cellulose suspension was transferred to the Ultrasound device after placing the sample in an ice bath and setting the device at 400 watts and 20 kHz for 30 min. In the next step, the samples were placed in a freeze at -20°C and transferred to a freeze-dryer at the College of Marine Sciences to obtain the nano-cellulose powder.

Both CMC and NCMC were prepared by two steps:

1- Alkalization pretreatment: Weigh 2 gm of cellulose or nano-cellulose, add 150 ml of isopropanol and 20 ml of (20% NaOH)

2- Etherification reaction: 3.5 gm of monochloroacetic acid was added to the mixture, and 200 ml of ethanol solution was added, and the pH was adjusted to (6-8) using acetic acid. The filtrate was then discarded, and the product was washed three times with ethanol solution and dried at 40°C for 24 hours.

The percentage of the Polymer yield was estimated using the following equation [8]:

$$\text{Polymer yield (\%)} = \frac{\text{polymer weight}}{\text{sample weight}} \times 100 \quad (1)$$

The active groups of polymers and nanopolymers were determined using the FT-IR (FT/IR-4100, Jasco, Japan), and the wavelength range was from 400-4000 cm^{-1}.

The crystallinity of polymers and nanopolymers was measured using an X-Ray Diffraction device (X-Pert pro), with an angle of 2Ɵ from 10 - 40 degrees. The degree of crystallinity of cellulose, cellulose nanopartiches, carboxymethyl cellulose and carboxymethyl cellulose nanoparticles was calculated according to Eq. (2) [9]:

$$CrI = (I_{(002)} - \frac{I_{(am)}}{I_{(002)}}) \times 100 \quad (2)$$

where CrI is the crystallinity index, $I_{(002)}$ is the peak of the crystallization curve at 2θ = 22-26, $I_{(am)}$ is the top of the curve for the amorphous diffraction at 2θ = 15-18.

The water binding capacity of carboxymethyl cellulose and carboxymethyl cellulose nanopartiches was estimated according to the method used by (No et al., 2000).

The data were statistically analyzed according to a Complete Randomized Design (CRD) using statistical program SPSS (2018). The results were compared using the t-teat test to compare some of the characteristics and the differences were statistically significant at the level of (0.05), and each experiment was repeated three times.

3. Results and Discussion

Figure (1) shows the average size of carboxymethyl cellulose extracted from rice shells, as the figure shows that the average size of natural carboxymethyl cellulose extracted from rice husks was 35.865.7 nm.

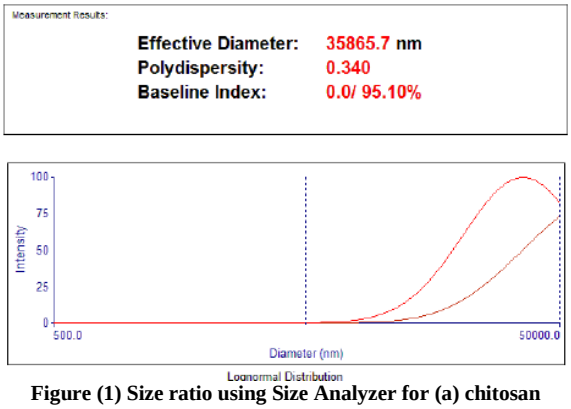

Figure (1) Size ratio using Size Analyzer for (a) chitosan extracted from shrimp shells (b) and cellulose extracted from rice shells

Figure (2) represents the infrared spectrum of samples of cellulose extracted from rice husks, nanocellulose, carboxymethyl cellulose CMC, and carboxymethyl cellulose nanocrystalline NCMC. Cellulose [10]. The presence of a low-intensity band at (2900.41-2921.63 cm^{-1}) for all samples is attributed to the C-H bond [11]. Also, the low intensity between 1500-1700 cm^{-1} in cellulose indicates the efficiency of the extraction process and the purity of the extracted cellulose, and the absence of amorphous lignin and hemicellulose compounds, which supports the results of XRD in high crystallinity of pure cellulose [12,13]. Infrared spectroscopy

examination of carboxymethyl cellulose and carboxymethyl cellulose nanoparticles shows the appearance of two bands at the frequency 1599.66 and 1645.95 cm^{-1}, respectively, which indicate C=O substituted carboxymethyl cellulose group, whose intensity was greater in NCMC than CMC, that supports the results of the degree of substitution for the mentioned samples which were 0.573 and 0.663, respectively [14]. Whereas the results of the same Figure showed the presence of bands between 1419.35 and 1427.07 cm^{-1}, and 1326.82 and 1370.18 cm^{-1}, which indicates the stretching vibration of the CH_2 and C-O-H, respectively, that indicates the loss of crystallization during the synthesis of carboxymethylation, which leads to a decrease in the band for the O-H at the frequency 3362.28-3428.8 cm^{-1} (Rashid and Dutta, 2022). The stretching vibration of the C-O-C bond in the pyranose ring in the cellulose of the samples under study, appeared at the frequency 1059.69-1119.48 cm^{-1} [15], and the stretching vibration of the β-1.4 bond appeared at the frequency 895.212-898.666 cm^{-1} [16].

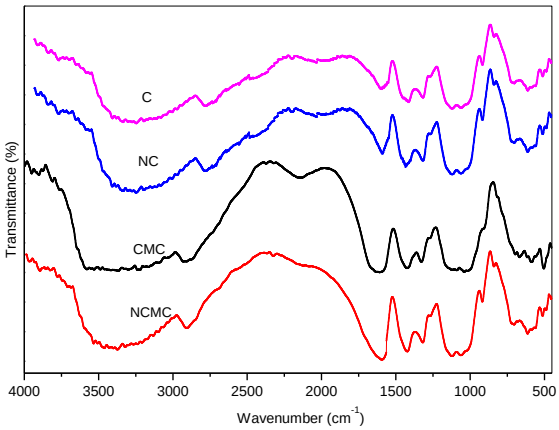

Fig. (2) FTIR spectrum of natural cellulose (C), nano-cellulose (NC), natural carboxymethyl cellulose(CMC) and nano carboxymethyl cellulose (NCMC)

Figure (3) shows the XRD of cellulose (C), nano-cellulose (NC), carboxymethyl cellulose (CMC), and carboxymethyl cellulose (NCMC), it is noticed that there are three distinct peaks at the diffraction angles (2θ) 16.18°, 22.63° and 34.03° for cellulose, and 16.23°, 22.41°, and 34.76° for nanocellulose. Also it observed that the crystallization disappeared for both CMC and NCMC and their transformation into the amorphous form due to cleavage of the hydrogen bonds of the -OH group and its replacement by the carboxymethyl group (-(CH_2-COOH)). As well as the breaking of hydrogen bonds when preparing CMC from cellulose in the basic environment (NaOH), which in turn leads to the disappearance of crystallization [17]. There were three peaks of cellulose at the diffraction angles (2θ) 16.4°, 22.3°, and 34.4° and the presence of the main peak of high density at the diffraction angle of 22.3° indicates the crystalline form of cellulose and the decrease in the degree of crystallization increases with the increase in the degree of substitution [18].

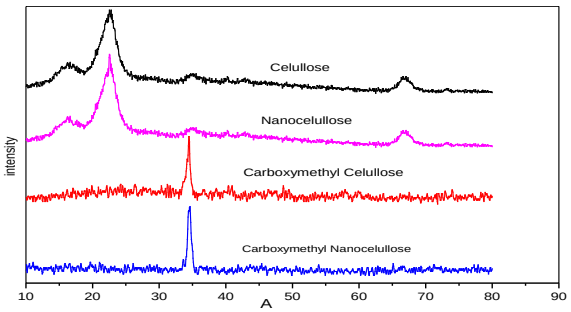

Fig. (3) XRD for cellulose (C), nanocellulose (NC), carboxymethyl cellulose (CMC), and carboxymethyl cellulose (NCMC)

4. Conclusion

Cellulose (C) was extracted from agricultural residues of rice husks and prepared nano-cellulose (NC), Carboxymethyl cellulose (CMC), and Carboxymethyl cellulose nanoparticles (NCMC). Results showed that no apparent differences in chemical composition between polymers and nanopolymers in addition to an increase in the crystallization index of cellulose nanoparticles the crystallization loss of Carboxymethyl cellulose and Carboxymethyl cellulose nanoparticles caused the replacement of the bonds in the hydroxyl group with a Carboxymethyl group (CH_2-COOH). The results show a decrease in the physical properties such as viscosity, water-binding capacity and fat-binding capacity for Carboxymethyl cellulose nanoparticles compared to natural polymers.

References

[1] H.P.S. Abulkalil, A.H. Bhat and A.F. Yasra, "Green composite from sustainable cellulose naon fibrils: A review", *Carbohyd. Polym. J.*, 87 (2012) 963-979.
[2] A. Ali and S. Ahmed, "A review on chitosan and its nanocomposites in drug delivery", *Int. J. Biolog. Macromol.*, 109 (2018) 273-286.
[3] N.D. Aljbour, M.D. Beg and J. Gimbun, "Acid hydrolysis of chitosan to oligomers using hydrochloric acid", *Chem. Eng. Technol.*, 42(9) (2019) 1741-1746.
[4] R.R. Andalia, J. Julinawati and H. Heliwati, "Isolation and characterization of cellulose from rice husk waste and sawdust with chemical method", *Jurnal Natural*, 20(1) (2020) 6-9.
[5] J. Araki, Y. Yamanaka and K. Ohkawa, "Chitin-chitosan nanocomposite gels: reinforcement of chitosan hydrogels with rod-like chitin nanowhiskers", *Polymer J.*, 44(7) (2012) 713-717.
[6] S.E.A.M. Asri et al., "Isolation and characterization of chitin nanowhiskers from fermented tiger prawn waste", *Chem. Eng. Trans.*, 56 (2017) 139-144.
[7] ASTM, 2005. Analytical method for determining Degree of substitution in the Product. Document CK-G06 Edition, 05: D-1439-03.
[8] S. Bano and Y.S. Negi, "Studies on cellulose nanocrystals isolated from groundnut shells", *Carbohyd. Polym.*, 157 (2017) 1041-1049.
[9] M.R. Barkhordari and M. Fathi, "Production and characterization of chitin nanocrystals from prawn shell and their application for stabilization of Pickering emulsions", *Food Hydrocoll.*, 82 (2018) 338-345.
[10] H. Bidgoli et al., "Preparation of carboxymethyl cellulose superabsorbents from waste textiles", *Fibers Polym.*, 15(3) (2014) 431-436.
[11] A. Bratovčić et al., "Application of polymer nanocomposite materials in food packaging", *Croatian J. Food Sci. Technol.*, 7(2) (2015) 86-94.
[12] L. Cao et al., "An edible oil packaging film with improved barrier properties and heat sealability from cassia gum incorporating carboxylated cellulose nano crystal whisker", *Food Hydrocoll.*, 98 (2020) 105251.
[13] D.P. Chattopadhyay and M.S. Inamdar, "Studies on synthesis, characterization and viscosity behaviour of nano chitosan", *Res. J. Eng. Sci.*, 1(4) (2012) 9-15.
[14] D.P. Chattopadhyay and B.H. Patel, "Synthesis, Characterization and Application of Nano cellulose for enhanced performance of textiles", *J. Textile Sci. Eng.*, 2 (2016) 248.
[15] S. Chen and D. Chen, "Surface deacetylation of chitin nano-whiskers", *Polym. Bull.*, 77(10) (2020) 5345-5355.
[16] S.P. Druzian et al., "Preparation of chitin nanowhiskers and its application for crystal violet dye removal from wastewaters", *Enviro. Sci. Pollut. Res.*, 26(28) (2019) 28548-28557.
[17] S. Gokila et al., "Removal of the heavy metal ion chromiuim (VI) using Chitosan and Alginate nanocomposites", *Int. J. Biolog. Macromol.*, 104 (2017) 1459-1468.
[18] S. Gopi et al., "Chitin nanowhisker–Inspired electrospun PVDF membrane for enhanced oil-water separation", *J. Enviro. Manag.*, 228 (2018) 249-259.

IRAQI JOURNAL OF APPLIED PHYSICS LETTERS
EDITORIAL BOARD

COPYRIGHT RELEASE FORM

IRAQI JOURNAL OF
APPLIED PHYSICS LETTERS (IJAPLett)

We, the undersigned, the author/authors of the article titled

……
……
……
……
……
……
……

that is submitted to the Iraqi Journal of Applied Physics Letters (IJAPLett) for publication, declare that we have neither taken part or full text from any published work by others, nor presented or published it elsewhere in any other journal. We also declare transferring copyrights and conduct of this article to the Iraqi Journal of Applied Physics Letters (IJAPLett) after accepting it for publication.

The authors will keep the following rights:

1. Possession of the article such as patent rights.
2. Free of charge use of the article or part of it in any future work by the authors such as books and lecture notes after informing IJAP editorial board.
3. Republishing the article for any personal purposes of the authors after taking journal permission.

To be signed by all authors:

Signature:……..date: ……
Printed name: ……

Signature:……..date: ……
Printed name: ……

Signature:……..date: ……
Printed name: ……

Correspondence author:……...
……
Address:……
……
Telephone:……..……..email: ……

Note: Complete and sign this form and mail it to the below address with your finally revised manuscript

The Iraqi Journal of Applied Physics Letters
ISSN (Print): 1999-656x, ISSN (Online): 2309-1673
www.iraqiphysicsjournal.com
Email: editor@iraqiphysicsjournal.com
Email: editor_ijap@yahoo.co.uk
Email: ijap.editor@gmail.com

IRAQI JOURNAL OF APPLIED PHYSICS LETTERS
Volume (5) Issue (4) October-December 2022

CONTENTS

The *Iraqi Journal of Applied Physics Letters (IJAPLett)* is a peer reviewed journal of high quality devoted to the publication of original research papers from applied physics and their broad range of applications. IJAPLett publishes quality original research letters in physics and its applications in the broadest sense. It is intended that the journal may act as an interdisciplinary forum for physics and its applications. Innovative applications and material that brings together diverse areas of physics are particularly welcome. IJAPLett aims to disseminate knowledge; provide a learned reference in the field; and establish channels of communication between academic and research experts, policy makers and executives in industry, commerce and investment institutions. IJAPLett is a quarterly specialized periodical dedicated to publishing original letters in: Applied & Nonlinear Optics, Applied Mechanics & Thermodynamics, Digital & Optical Communications, Electronic Materials & Devices, Laser Physics & Applications, Plasma Physics & Applications, Quantum Physics & Spectroscopy, Semiconductors & Optoelectronics, Solid State Physics & Applications, Alternative & Renewable Energy, and Environmental Science & Technology.

Sponsored and Published by
Iraqi Society for Alternative and Renewable Energy Sources and Techniques

Co-published by
American Quality for Scientific Publishing